Energy & Environmental Science

ROYAL SOCIETY OF CHEMISTRY

PAPER

Published on 07 July 2026

Cite this: DOI: 10.1039/d6ee01246a

A novel carborane-based electron transport material for high-performance perovskite/silicon tandem solar cells

Lea Zimmermann, [a] Julius Petrulevicius, [b] Dorothee Menzel, [a] Wander Max Bernardes de Araujo, [a] Kazuki Morita, [a] Suresh Maniyarasu, [a] Maxim Simmonds, [a] Yasaman Salimi, [c] Dong Kuk Kim, [d] Florian Mathies, [a] Florian Scheler,[a] Sebastian Berwig, [a] Woongmo Sung, [e] Satoshi Nihonyanagi, [ef] Arman Mahboubi Soufiani, [a] Angelika Harter, [a] Vygintas Jankauskas, [g] Jona Kurpiers, [a] Tadas Malinauskas, [b] Tahei Tahara, [e] Mariadriana Creatore, [ch] Sebastian Wood, [d] Rutger Schlatmann, [ai] Bernd Stannowski, [a] Lars Korte, [a] Eike Köhnen, [a] Vytautas Getautis [b] and Steve Albrecht*[aj]

The fullerene C_{60} is the prevalent electron transport material (ETM) in high-efficiency perovskite/silicon tandem solar cells. However, it introduces intrinsic limitations, including high interfacial non-radiative recombination losses, the formation of mechanically weak interfaces, and high parasitic absorption. Here, we report a non-fullerene ETM based on a *meta*-carborane core and 9-fluorenylidene malononitrile functional groups (mCB-FMN) that addresses these challenges while maintaining the processing advantages of C_{60}. Thermally evaporated mCB-FMN forms uniform, conformal thin films that enable efficient electron extraction and strongly suppress interfacial non-radiative recombination losses compared to C_{60}. The introduction of this novel ETM further reduces oxygen-induced degradation of the perovskite/ETM interface, improves the nucleation of the SnO_x buffer layer grown by atomic layer deposition and enhances interfacial adhesion within the perovskite/ETM/SnO_x stack. Its wide optical bandgap is another key advantage, as it minimizes parasitic absorption losses in tandem solar cells. Replacing C_{60} with mCB-FMN in opaque p–i–n perovskite single-junction devices improves the power conversion efficiency (PCE) by 1.5% (absolute), driven by a 110 meV increase in open-circuit voltage (V_{OC}). Proof-of-concept perovskite/silicon tandem integration of mCB-FMN yields a PCE of 31.3%, surpassing the C_{60}-based reference by 2.4% (absolute) through simultaneous improvements in V_{OC} and short-circuit current density. These results establish mCB-FMN as a novel non-fullerene ETM for perovskite/silicon tandem solar cells that overcomes the performance limitations of conventional C_{60} and highlight carborane-based compounds as a promising new class of materials for high-efficiency perovskite photovoltaics.

Received 25th February 2026,
Accepted 18th June 2026

DOI: 10.1039/d6ee01246a

rsc.li/ees

Broader context

Perovskite solar cells have emerged as a highly promising photovoltaic technology due to their low production costs and exceptional power conversion efficiencies, exceeding 27% for single-junction devices and 35% for perovskite/silicon tandems. To date, all published record-efficiency p–i–n perovskite/silicon

[a] *Solar Energy Division, Helmholtz-Zentrum Berlin, Berlin, 12489, Germany. E-mail: steve.albrecht@helmholtz-berlin.de*
[b] *Department of Organic Chemistry, Kaunas University of Technology, Kaunas, 50254, Lithuania*
[c] *Department of Applied Physics and Science Education, Eindhoven University of Technology, Eindhoven, 5600 MB, The Netherlands*
[d] *Electromagnetic and Electrochemical Technologies Department, National Physical Laboratory, Teddington, Middlesex, TW11 0LW, UK*
[e] *Molecular Spectroscopy Laboratory, RIKEN, Wako, Saitama 351-0198, Japan*
[f] *Department of Chemistry, Institute of Pure and Applied Sciences, University of Tsukuba, Tsukuba, Ibaraki 305-8571, Japan*
[g] *Institute of Chemical Physics, Vilnius University, Vilnius, 10257, Lithuania*
[h] *Eindhoven Institute of Renewable Energy Systems (EIRES), Eindhoven, 5600 MB, The Netherlands*
[i] *School of Engineering – Energy and Information, Hochschule für Technik und Wirtschaft, Berlin, 10313, Germany*
[j] *Fakultät IV – Elektrotechnik und Informatik, Technische Universität Berlin, Berlin, 10587, Germany*

tandem solar cells have incorporated the fullerene C_{60} or its derivatives as electron transport material (ETM). However, C_{60} presents several challenges, including high interfacial non-radiative recombination losses, high material costs, and the formation of mechanically weak interfaces. Additionally, its interaction with ambient oxygen can impair device performance, while its high parasitic absorption reduces photocurrent in perovskite/silicon tandem solar cells. In light of these limitations, there is growing interest in non-fullerene ETMs. However, most studies to date have focused on single-junction devices with low-bandgap perovskites, which impose less demanding requirements on charge-carrier selectivity and optical properties, and/or have relied on solution-based deposition methods, thereby limiting their suitability for large-area fabrication and compatibility with textured perovskite surfaces. Here we introduce a novel carborane-based ETM as a complete replacement for fullerene ETMs, overcoming the key limitations of C_{60} while retaining compatibility with vacuum processing and enabling integration with wide-bandgap perovskite absorbers for perovskite/silicon tandems. This work establishes a fundamentally new materials concept and represents the first successful integration of a high-performance fullerene replacement in monolithic p–i–n perovskite/silicon tandem solar cells.

1. Introduction

State-of-the-art p–i–n perovskite single-junction and multi-junction solar cells rely on C_{60} as the electron transport material (ETM),[1–5] leveraging its ability to rapidly extract electrons from the perovskite absorber,[6,7] its high electron mobility,[8] and its compatibility with thermal evaporation allowing for the deposition of thin, conformal layers over large substrate areas.[9] To date, almost all published record-efficiency p–i–n perovskite/silicon tandem solar cells have incorporated this ETM.[2,10–17] However, C_{60} presents several challenges, including high non-radiative recombination losses at the perovskite/C_{60} interface that limit the device's open-circuit voltage (V_{OC}),[18] high material costs,[19] and the formation of mechanically weak interfaces prone to delamination.[20,21] Additionally, its interaction with ambient oxygen can impair device performance,[9,22,23] while its high parasitic absorption reduces the photocurrent in architectures where light enters through the ETM, as is the case in perovskite/silicon tandem solar cells.[24] Although, depending on the perovskite composition, C_{60} derivatives such as phenyl-C_{61}-butyric acid methyl ester (PCBM) can offer improvements, such as enhanced energetic alignment and defect passivation,[6,25,26] they do not fully resolve inherent limitations of pristine C_{60} and are typically restricted to solution-based deposition methods. Most commonly, high non-radiative recombination losses at the perovskite/C_{60} interface are addressed by introducing passivating interlayers and/or perovskite surface treatments. While effective, these strategies require the deposition of additional layers, increasing fabrication complexity, and potentially compromise device stability.[15,27,28]

Due to these limitations, there is growing interest in alternative non-fullerene ETMs.[29] Feng *et al.*[30] recently reported a spin-coated cyano-functionalized bithiophene imide polymer (PCNI2-BTI), which exhibited excellent electron transport properties due to favorable molecular orientation and stacking on the perovskite surface. Huang *et al.*[31] introduced Y-type non-fullerene acceptors, namely Y-Phen and Y-CE, inspired by Y6 structures widely used in bulk heterojunction organic solar cells. Solution-processed Y-CE enabled efficient charge extraction and transport due to ordered molecular assembly and enhanced packing on the perovskite. In addition, small-molecule electron acceptors such as perylene diimide (PDI), naphthalene diimide (NDI), and hexaazatrinaphthylene (HATNA) derivatives have been explored as ETMs in perovskite photovoltaics.[32–38] Originally developed for organic solar cells, these molecules possess rigid, extended π-conjugated backbones and high electron affinities, enabling efficient charge extraction and transport. Metal oxide-based electron transport layers, such as SnO_x, offer an alternative approach to replacing fullerene-based ETMs. In this context, Gao *et al.*[39] demonstrated fullerene-free devices by tuning oxygen vacancy defects in the SnO_x layer by adjusting the atomic layer deposition (ALD) process and incorporating a spin-coated organic passivation layer. In another study, Kim *et al.*[40] employed spin-coated SnO_2 quantum dots on an ethylenediamine-treated wide-bandgap perovskite (1.77 eV), yielding 27.0% power conversion efficiency (PCE) in four-terminal all-perovskite tandem devices.

While the above-mentioned studies demonstrate the potential of non-fullerene ETMs, most have focused on single-junction devices with low-bandgap perovskites. The use of non-fullerene ETMs in combination with wider-bandgap perovskites suitable for perovskite/silicon tandem solar cells remains largely unexplored. The requirements for ETMs in tandem architectures are particularly demanding, as they must not only ensure sufficient charge carrier selectivity (*i.e.*, hole-blocking ability) but also feature minimal parasitic absorption.[29] Additionally, many of the reported non-fullerene ETMs rely on solution-based deposition methods such as spin-coating, which limit their suitability for large-area fabrication and compatibility with textured perovskite surfaces, thereby restricting their industrial applicability. In contrast, thermal evaporation enables the deposition of thin films with precise thickness control, excellent uniformity, and good scalability, even on rough or textured substrates. These characteristics make it a preferred method for depositing charge transport layers in perovskite solar cells, supporting both laboratory-scale and large-scale industrial manufacturing. Moreover, since C_{60} is typically processed *via* thermal evaporation, an effective alternative ideally should exhibit similar compatibility to allow straightforward integration into existing processes.

A particularly interesting class of materials for application as an ETM in perovskite solar cells is that of closo-carboranes. These cage-like, spherical molecules, composed of carbon, boron, and hydrogen, feature an icosahedral geometry and exhibit three-dimensional aromaticity, which contributes to their exceptional chemical and thermal stability.[41] Carborane-based compounds have been applied in various optoelectronic devices, including organic light-emitting diodes (OLEDs),[42–44] organic solar cells,[41] and organic field-effect transistors,[45] in which their tunable electronic properties have been exploited. In the context

of perovskite photovoltaics, carborane-based molecules have been employed in a broad range of applications: as an interfacial passivation layer at the perovskite/C_{60} interface to suppress non-radiative recombination losses,[46] as a post-treatment on top of the perovskite/PCBM stack to simultaneously improve the contact to the Ag electrode and passivate the perovskite bulk,[47] as a p-contact interlayer in all-perovskite tandem solar cells to enhance heat dissipation and improve thermal regulation,[48] and as part of a bilayer hole-transporting contact in combination with PEDOT:PSS.[49] Notably, in all these implementations, carborane-based materials have been employed as interfacial modifiers or auxiliary layers rather than as stand-alone charge transport materials.

In this work, we introduce a novel ETM based on a *meta*-carborane core and 9-fluorenylidene malononitrile functional groups (mCB-FMN, Fig. 1a), synthesized from commercially available reagents *via* a simple three-step synthesis route (Fig. S1). This thermally evaporated ETM overcomes key limitations of C_{60} by offering increased mechanical adhesion of the perovskite/ETM/SnO_x stack, reduced nucleation delay of ALD-grown SnO_x, and enhanced stability against air-induced degradation. It further substantially improves the V_{OC} compared to C_{60} by suppressing interfacial non-radiative recombination losses and additionally boosts the short-circuit current density (J_{SC}) in devices that are illuminated through the ETM owing to its wide optical bandgap.

2. Results and discussion

2.1. Suitability for thermal evaporation and optoelectronic properties

First, we evaluated the suitability of mCB-FMN for deposition *via* thermal evaporation. To this end, thermogravimetric analysis (TGA) was performed under ambient pressure. As shown in Fig. 1b, the compound exhibited a sharp weight loss onset and a 5% weight loss temperature of 386 °C, indicating sufficient thermal stability for vacuum-based deposition. Under typical process pressures (1×10^{-6} to 3×10^{-6} mbar), mCB-FMN sublimes at 160–180 °C, enabling deposition rates of 0.1–0.2 Å s^{-1} at significantly lower temperatures than those required for C_{60} (>330 °C). The reduced sublimation temperature offers practical advantages for vacuum processing, including lower energy consumption, as well as decreased thermal stress on the evaporator system components.

To assess the charge transport properties of the carborane-based ETM, its electron mobility was determined by xerographic time-of-flight (XTOF) measurements (Fig. 1c). mCB-FMN exhibited

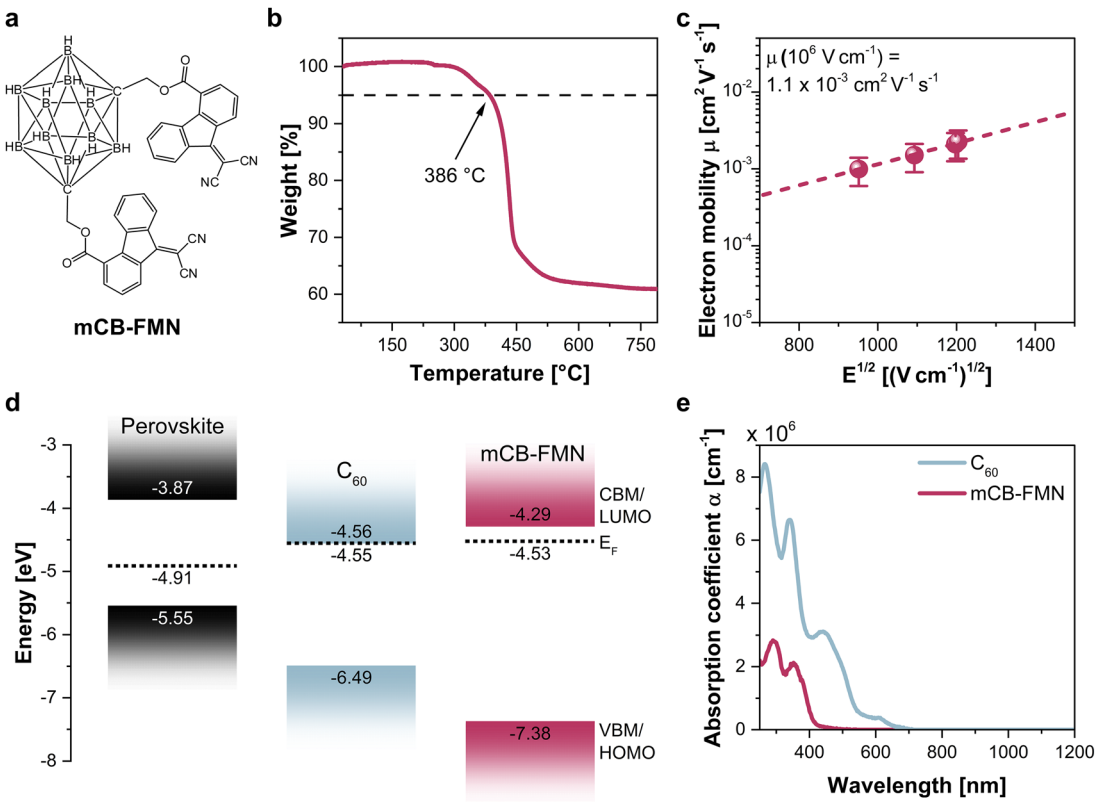

Fig. 1 Suitability of mCB-FMN for thermal evaporation and optoelectronic properties. (a) Molecular structure of mCB-FMN. (b) TGA of mCB-FMN. (c) Field-dependent electron mobility μ of mCB-FMN determined by XTOF measurements. (d) Energy levels of the perovskite, C_{60} and mCB-FMN (referenced to the vacuum level at 0 eV). The VBM/HOMO and E_F positions were determined by He-UPS measurements of the individual layers deposited on glass/ITO. The CBM/LUMO positions of C_{60} and mCB-FMN were calculated based on the VBM/HOMO level and the optical bandgap determined by spectral absorption measurements. (e) Spectral absorption coefficient α of C_{60} and mCB-FMN determined from the spectral absorption of thin films on quartz glass.

an electron mobility of 1.1×10^{-3} $cm^2 V^{-1} s^{-1}$ at an applied field of 10^6 V cm^{-1}, and a low Poole–Frenkel slope ($\alpha = 0.0032$ cm $V^{-1/2}$), indicating relatively field-insensitive charge transport. Comparing the electron mobility of mCB-FMN with the widely used ETM PCBM reveals a significantly lower mobility for mCB-FMN (approximately three orders of magnitude at zero field, estimated from linear fits of the data sets, see Fig. S2). Since the electron mobility of C_{60} exceeds that of PCBM,[8] the disparity between mCB-FMN and C_{60} is likely even larger. This implies that, in solar cells, only thin layers of mCB-FMN should be employed where the electron mobility for vertical transport is not expected to limit device performance.

Another key parameter determining the suitability of a material as an ETM is its energetic alignment with the perovskite absorber, as it directly impacts charge carrier dynamics at the interface. To this end, the valence band maximum (VBM)/highest occupied molecular orbital (HOMO) and Fermi level positions of the 1.68 eV triple-cation triple-halide perovskite ($Cs_{0.22}FA_{0.78}Pb(I_{0.85}Br_{0.15})_3$ + 5% $MAPbCl_3$), C_{60}, and mCB-FMN were determined by He-I ultraviolet photoemission spectroscopy (He-UPS) performed on the individual layers on glass/ITO (see secondary electron cut-off (SECO) and HOMO regions in Fig. S3). We note that the energetics of the formed interface may deviate from those inferred from the individual layers. In addition, illumination-induced surface photovoltage (SPV) can affect the measured Fermi level position of photoactive perovskite layers.[50] The lowest unoccupied molecular orbital (LUMO) levels of C_{60} and mCB-FMN were estimated based on their HOMO levels combined with the corresponding optical bandgaps (see below). It should be considered that optical bandgaps may differ from the corresponding electrical bandgaps, potentially leading to deviations in the absolute LUMO positions. As illustrated in the energy level diagram (Fig. 1d), mCB-FMN displays n-type character, with a slightly higher-lying LUMO compared to C_{60} and a deep-lying HOMO (relative to the vacuum level). The relative energetic positions may facilitate electron extraction from the perovskite to mCB-FMN. The deep-lying HOMO level further enhances hole-blocking, thereby improving the charge carrier selectivity compared to C_{60}. This further offers potential compatibility with even wider-bandgap perovskites (>1.68 eV), such as those used in all-perovskite tandem or triple-junction solar cells.

For applications in p–i–n stacked perovskite/silicon tandem solar cells, the optical properties of the ETM are particularly relevant, as light enters the device through the electron-selective top contact. Ultraviolet-visible-near-infrared (UV-Vis-NIR) spectroscopy reveals that mCB-FMN exhibits a low absorption coefficient in the relevant wavelength range and a wide optical bandgap of 3.09 eV (Fig. 1e and Fig. S4). For comparison, C_{60} shows a significantly narrower bandgap of 1.92 eV. Accordingly, replacing C_{60} with mCB-FMN in perovskite/silicon tandem solar cells offers the potential to substantially reduce parasitic absorption in the top contact and is expected to enable higher photocurrent generation in the perovskite top cell.

2.2. Charge carrier dynamics at the perovskite/ETM interface

To assess charge carrier dynamics at the perovskite/ETM interface, transient surface photovoltage (trSPV) measurements were performed. The transients (Fig. 2a) reveal fast extraction of electrons for the sample based on perovskite/C_{60}, evident as rapid increase in the negative SPV amplitude after excitation with a 700 nm laser. Consistent with the favorable energetic alignment discussed above, efficient electron extraction is also observed for the perovskite/mCB-FMN layer stack. In particular, at early times ($<2.5 \times 10^{-8}$ s), both mCB-FMN and C_{60} exhibit similar slopes, indicating comparable initial charge extraction rates. However, the C_{60}-based sample reaches its maximum SPV amplitude at earlier times compared to the mCB-FMN partial stack sample ($\sim 7 \times 10^{-8}$ s *vs.* $\sim 10^{-6}$ s, respectively). This difference arises from the higher overall SPV amplitude with mCB-FMN as ETM, which, at comparable extraction rates, leads to a longer rise time to reach the maximum signal, together with a slightly reduced slope at times $>2.5 \times 10^{-8}$ s. The moderately slower dynamics at $>2.5 \times 10^{-8}$ s may originate from the different energetic alignment at the perovskite/ETM interface compared to C_{60}[51] and/or slower electron transport to the surface as a result of the lower electron mobility of mCB-FMN. The substantially enhanced SPV amplitude, on the other hand, suggests improved carrier separation and/or an increased excess carrier density, for example, due to reduced interfacial non-radiative recombination. A reduction in non-radiative recombination is further supported by both transient and steady-state photoluminescence (PL) measurements. Transient PL measurements reveal increased differential decay times for perovskite/mCB-FMN samples compared to those with C_{60} (Fig. S5). In steady-state PL measurements, mCB-FMN yields a markedly higher PL emission and an increase in the quasi-Fermi level splitting (QFLS) by 70 meV relative to C_{60} (Fig. 2b and Fig. S6). Notably, the QFLS of the solar cell partial stack (ITO/self-assembled monolayer (SAM)/perovskite) decreases by only 30 meV with the addition of the mCB-FMN layer, in contrast to a 100 meV reduction observed when the C_{60} ETM is introduced (Fig. S6). These results suggest that mCB-FMN effectively mitigates one of the key limitations of C_{60} – namely, high interfacial non-radiative recombination – without the need for an additional passivation layer.

A proposed origin of non-radiative recombination losses in perovskite solar cells incorporating C_{60} is the energetic offset between the perovskite CBM and the C_{60} LUMO level.[50,51] As shown in Fig. 1d, this offset is reduced in the case of mCB-FMN, which may contribute to the suppression of non-radiative recombination and the enhanced QFLS. However, it is worth noting that estimating the energetic alignment at a heterointerface based on measurements of individual layers does not account for possible interfacial effects such as chemical bonding, the formation of interface dipoles, or orbital hybridization.

To further investigate possible interfacial effects, we performed density functional theory (DFT) calculations on a simplified $FAPbI_3$ perovskite surface slab as a representative model system with a single mCB-FMN or C_{60} molecule on the surface. In the most stable configuration, mCB-FMN is positioned flat on a PbI_2-terminated perovskite surface, with both FMN units oriented parallel to the surface (Fig. 2c). The CN group of the FMN moiety closer to the perovskite interface coordinates to an

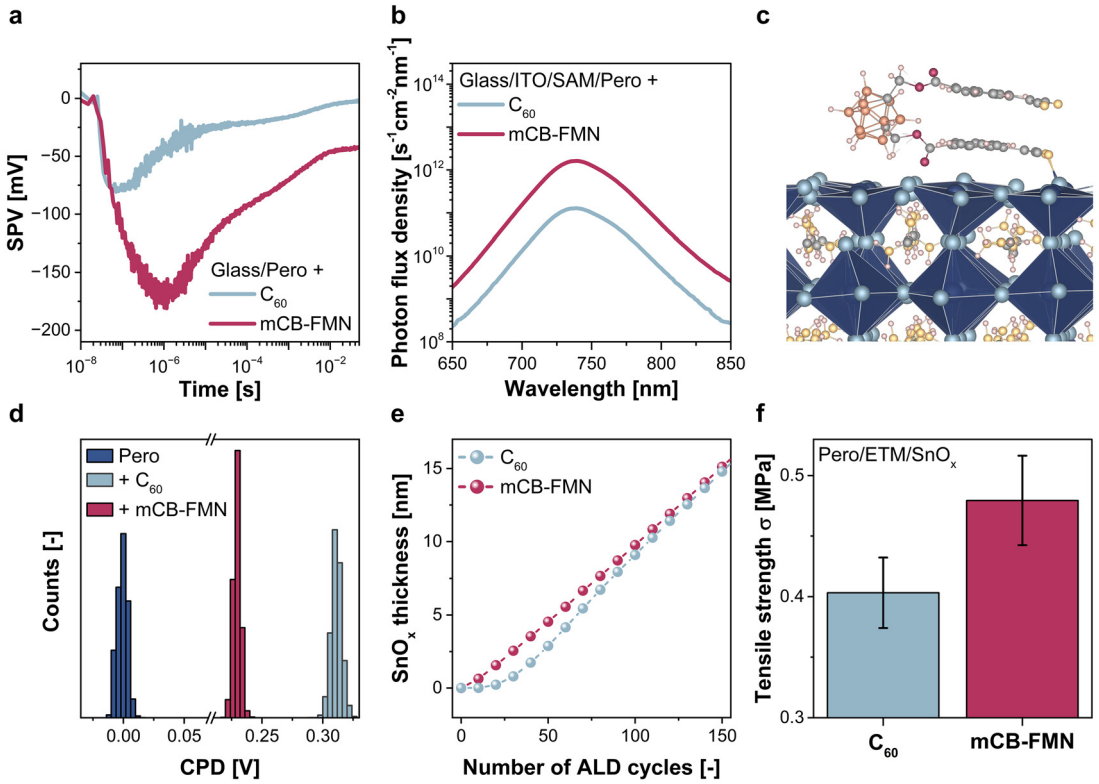

Fig. 2 Charge carrier dynamics, surface properties, and mechanical stability. (a) SPV transients of solar cell half-stacks (glass/perovskite/ETM). (b) Photon flux densities from steady-state PL measurements of solar cell partial stacks (glass/ITO/SAM/perovskite/ETM). (c) DFT-calculated configuration of mCB-FMN on a PbI_2-terminated $FAPbI_3$ perovskite surface slab model. (d) Histogram of CPD values from KPFM measurements on a (5 × 5) μm^2 area on samples consisting of glass/ITO/SAM/perovskite with 16 nm C_{60} or 4 nm mCB-FMN. (e) Evolution of SnO_x thickness with ALD cycle number on mCB-FMN- and C_{60}-covered Si substrates, obtained from *in situ* ellipsometry, using an ALD process temperature of 80 °C. The graph shows an excerpt of the first 150 cycles of the experiment. (f) Tensile strength σ of solar cell partial stacks (glass/ITO/SAM/perovskite/ETM/SnO_x). The bars indicate the mean value of six samples per ETM and the corresponding standard deviation.

undercoordinated Pb^{2+} site. The resulting binding energy of −1.72 eV is significantly larger in magnitude than that calculated for C_{60} (−0.98 eV, Fig. S7). This preferentially flat orientation of mCB-FMN on the perovskite surface is further consistent with results from heterodyne-detected vibrational sum frequency generation (HD-VSFG) spectroscopy (see Note S7 and Fig. S8).

Our DFT calculations further show that mCB-FMN can interact with Pb_I antisite defects on the perovskite surface. These point defects, although supposedly present at a low density, are expected to introduce deep defect states in the perovskite bandgap and may act as effective non-radiative recombination centers.[52–54] The calculations confirm that Pb_I antisites at the surface give rise to deep electronic states and induce significant lattice distortion. Upon interaction with mCB-FMN, this distortion is partially relaxed, and the associated defect level shifts closer to the CBM (Fig. S9 and S10). This could contribute to a reduction in non-radiative recombination compared to C_{60}, as observed experimentally.

2.3. Layer properties, SnO_x growth, and mechanical stability

To gain insight into the chemical composition of the evaporated mCB-FMN films, we performed X-ray photoelectron spectroscopy (XPS) measurements on a 10 nm mCB-FMN layer deposited on glass/ITO. The sample exhibited the characteristic B 1s, C 1s, N 1s, and O 1s core-level signals corresponding to the molecular structure of mCB-FMN (Fig. S11). We further recorded XPS spectra for mCB-FMN layers with thicknesses ranging from 0 to 10 nm deposited on top of the perovskite. All mCB-FMN-related core-level signals were also clearly present when the ETM was deposited on the perovskite, with no discernible differences that would indicate changes in the chemical bonds. With increasing mCB-FMN thickness, the perovskite-related peaks progressively diminish, while the signals characteristic of mCB-FMN increase, consistent with the expected attenuation of perovskite photoelectrons (Fig. S11).

To identify the optimal thickness of mCB-FMN for device integration, we systematically varied the thickness of the thermally evaporated layer between 2 and 8 nm in opaque single-junction devices (Fig. S12). The highest PCE was achieved at a thickness of 4 nm. Devices with a 2 nm mCB-FMN layer exhibited reduced V_{OC} values, supposedly due to insufficient coverage of the ETM, whereas thicker layers led to a higher series resistance (Fig. S13) and therefore to a reduced FF, which may be attributed to the low electron mobility of the material. Accordingly, a thickness of 4 nm represents the optimum, balancing high V_{OC} values with minimal transport losses. The previously optimized thickness of the C_{60} layer in perovskite/silicon tandem solar cells is 16 nm.[10]

Accordingly, the fourfold reduction in layer thickness of mCB-FMN also offers practical advantages such as low material consumption and reduced processing time at similar deposition rates. Moreover, fullerene ETMs currently represent a major cost factor in perovskite-based solar cells.[19,55,56] We therefore carried out a cost estimation for the synthesis of mCB-FMN at a 1 kg scale to obtain a theoretical market price and compared it with that of C_{60}. Based on this estimation, replacing 16 nm C_{60} with 4 nm mCB-FMN could lower the ETM-related material costs by more than 50% at the device level (see detailed information in Note S8).

To investigate the morphology of the thin mCB-FMN layer in comparison to C_{60}, we performed top-view scanning electron microscopy (SEM) on the bare perovskite and the perovskite coated with the respective ETMs. As depicted in Fig. S14, samples with 16 nm C_{60} exhibit small features on top of the perovskite grains that can be attributed to C_{60} and resulting in a rougher appearance compared to the bare perovskite. In contrast, the 4 nm mCB-FMN layer does not introduce discernible surface features; instead, the images are consistent with a uniform and conformal coating of mCB-FMN on top of the perovskite layer.

Surface topography maps from Kelvin probe force microscopy (KPFM) measurements (Fig. S15) confirm the observations, revealing small topographic features on top of the larger perovskite grains for the layer stack consisting of perovskite/C_{60}, accompanied by a slight increase in root mean square (RMS) roughness compared to the bare perovskite from 22.9 nm to 23.9 nm. In contrast, adding 4 nm of mCB-FMN on the perovskite resulted in no noticeable changes in surface morphology, while the RMS roughness only marginally increased to 23.6 nm. KPFM contact potential difference (CPD) maps show a distinct increase in the mean CPD upon addition of the ETMs on the perovskite by 310 mV and 230 mV for C_{60} and mCB-FMN, respectively. As depicted in Fig. 2d, both ETM-coated samples exhibit a narrow CPD distribution, reflecting uniform electronic properties across the surface and indicating homogeneous ETM layers.

To further investigate the surface properties of the ETM-covered perovskite layers, we performed contact angle measurements on samples consisting of glass/ITO/SAM/perovskite/ETM. These revealed a less hydrophobic and more polar surface character for mCB-FMN compared to C_{60} (Fig. S16 and Table S3). Moreover, similar contact angles for 4 nm and 16 nm mCB-FMN indicate that the surface properties are already governed by mCB-FMN at a thickness of 4 nm. This supports our previous observations of homogeneous mCB-FMN coverage at this low layer thickness.

The increased surface polarity could further indicate a higher density of nucleation sites for the growth of SnO_x by ALD on mCB-FMN compared to C_{60}. SnO_x is a critical component in perovskite/silicon tandem solar cells: it enables sputter deposition of the transparent conductive oxide (TCO) front contact by protecting the underlying layers from sputter-induced damage[57] and provides an internal barrier that can reduce stability-deteriorating diffusion processes to and from the perovskite absorber.[58] Poor and delayed growth of SnO_x by ALD on C_{60}, apparent as sub-surface growth and the initial formation of SnO_x islands instead of a continuous layer, has been reported and is commonly attributed to a low density of reactive nucleation sites on the C_{60} surface.[23,59–61] In contrast, mCB-FMN, with its 9-fluorenylidene malononitrile functional groups featuring nitrile (C$\equiv$N) and ester moieties (–COO–), may provide more favorable interaction sites for ALD precursors and thereby facilitate the initial nucleation of SnO_x. To investigate the SnO_x growth by ALD, we performed *in situ* spectroscopic ellipsometry measurements on crystalline silicon substrates covered with mCB-FMN or C_{60}. A growth delay of approximately 20 cycles was observed for C_{60}, in line with previous reports,[62] whereas this delay was absent for mCB-FMN (Fig. 2e and Fig. S17a). Moreover, stabilization of the growth per cycle (GPC), indicative of the onset of layer-by-layer growth, occurred after approximately 30 and 70 cycles for mCB-FMN and C_{60}, respectively (Fig. S17b). To further probe the initial stages of SnO_x growth, we conducted XPS measurements on samples consisting of glass/ITO/15 nm C_{60} or mCB-FMN after 5 and 10 SnO_x ALD cycles. As shown in Fig. S18, clear differences in the SnO_x-related signals could be observed. In particular, under identical measurement conditions, the Sn 3d peak area was 4.4- and 5.7-fold higher for mCB-FMN than for C_{60} after 5 and 10 ALD cycles, respectively. The O 1s signals associated with SnO_x show a similar trend. This indicates increased SnO_x coverage and/or thicker SnO_x layers at early growth stages and supports improved SnO_x nucleation on mCB-FMN, consistent with the *in situ* ellipsometry results. We further confirmed the improved ALD SnO_x growth characteristics at later stages by SEM imaging of SnO_x films grown on perovskite/ETM stacks. We therefore deposited SnO_x with 75 and 139 ALD cycles, corresponding to approximately 10 nm and 20 nm, respectively, as used in solar cells. The images indicate delayed island growth on C_{60}, with discontinuous SnO_x coverage after 75 cycles and full coalescence after 139 cycles. In contrast, SnO_x deposited on mCB-FMN shows significantly smaller grain features with no visible discontinuities even after just 75 cycles, and minimal differences between the two thicknesses (Fig. S19). Note that the depositions for *in situ* ellipsometry were performed in a different ALD system than the SnO_x layers analyzed by XPS and SEM. Accordingly, slight variations in the growth parameters and GPC were observed; however, the overall trend remains consistent.

Another key limitation of the C_{60} ETM is its poor adhesion and mechanical stability, which can lead to delamination of the top contact layers, particularly during encapsulation, module integration, or upon operational stress conditions, ultimately causing irreversible performance degradation.[20,21,63,64] As described above, DFT calculations indicate a substantially stronger interaction between the perovskite and mCB-FMN compared to C_{60}. This suggests that mCB-FMN may offer improved adhesion and mechanical stability. We therefore experimentally assessed the mechanical integrity by conducting tensile strength measurements on as-prepared solar cell partial stacks (glass/ITO/SAM/perovskite/ETM/SnO_x). While these measurements do not capture the evolution of adhesion under

operational stress or ageing conditions, improved initial mechanical robustness may still contribute to enhanced resistance against delamination-related degradation. Stacks incorporating mCB-FMN exhibited a tensile strength of 0.48 MPa, representing a 20% increase compared to C_{60}-based stacks (0.40 MPa), indicative of enhanced mechanical robustness (Fig. 2f). Consistent with previous reports,[20,21,63] SEM and XPS analyses of the samples after the adhesion test reveal mainly adhesive failure at the C_{60}/SnO_x interface and isolated cohesive failure of the C_{60} layer itself (Fig. S21 and S23a, b). For samples with mCB-FMN, the analyses similarly reveal delamination of the SnO_x layer along with partial removal of the mCB-FMN layer from the perovskite (Fig. S22, S23c, d and S24). Since the ETM/SnO_x interface appears to be the primary failure point for both ETMs, the improved mechanical stability with mCB-FMN most likely arises from enhanced adhesion at the mCB-FMN/SnO_x interface, which may be directly linked to the improved SnO_x growth characteristics. Additional adhesion tests on solar cell partial stacks without a SnO_x layer, *i.e.*, glass/ITO/SAM/perovskite/ETM, exhibited higher tensile strength than samples containing SnO_x, with failure occurring at the ITO/SAM/perovskite interface (Fig. S25 and S26). This indicates that, for both ETMs, mechanical integrity is not primarily limited by the perovskite/ETM interface but, depending on the layer stack, rather by the hole transport layer side or the ETM/SnO_x interface. A detailed description of the mechanical stability tests is provided in Note S9.

2.4. Single-junction solar cell performance, ETM fragment test, and carborane core series

Photovoltaic performance was evaluated in opaque single-junction perovskite solar cells based on the device architecture: glass/ITO/SAM/perovskite/ETM/SnO_x/Ag (0.1 cm^2 aperture area, Fig. 3e). For a direct comparison, devices were fabricated under identical conditions, with differences only in the ETM and its thickness. Furthermore, thermal evaporation of both ETMs was carried out under similar deposition rates and process pressures, as detailed in the methods section of the supplementary information, and no additional passivation layers were used in either case. Replacing the conventional 16 nm C_{60} layer with a 4 nm mCB-FMN film resulted in a notable increase in median V_{OC} by 110 mV, from 1.14 V to 1.25 V (Fig. 3d). This enhancement is consistent with the reduction in interfacial non-radiative recombination, as discussed above. Concurrently, a modest reduction in FF of 2.3% (absolute) was observed (Fig. 3c), which aligns with the lower electron mobility in this material. The J_{SC} remained virtually unchanged (Fig. 3b), as expected under illumination through the p-type contact, and was confirmed by external quantum efficiency (EQE) measurements (Fig. S27). Despite the decrease in FF, the overall PCE

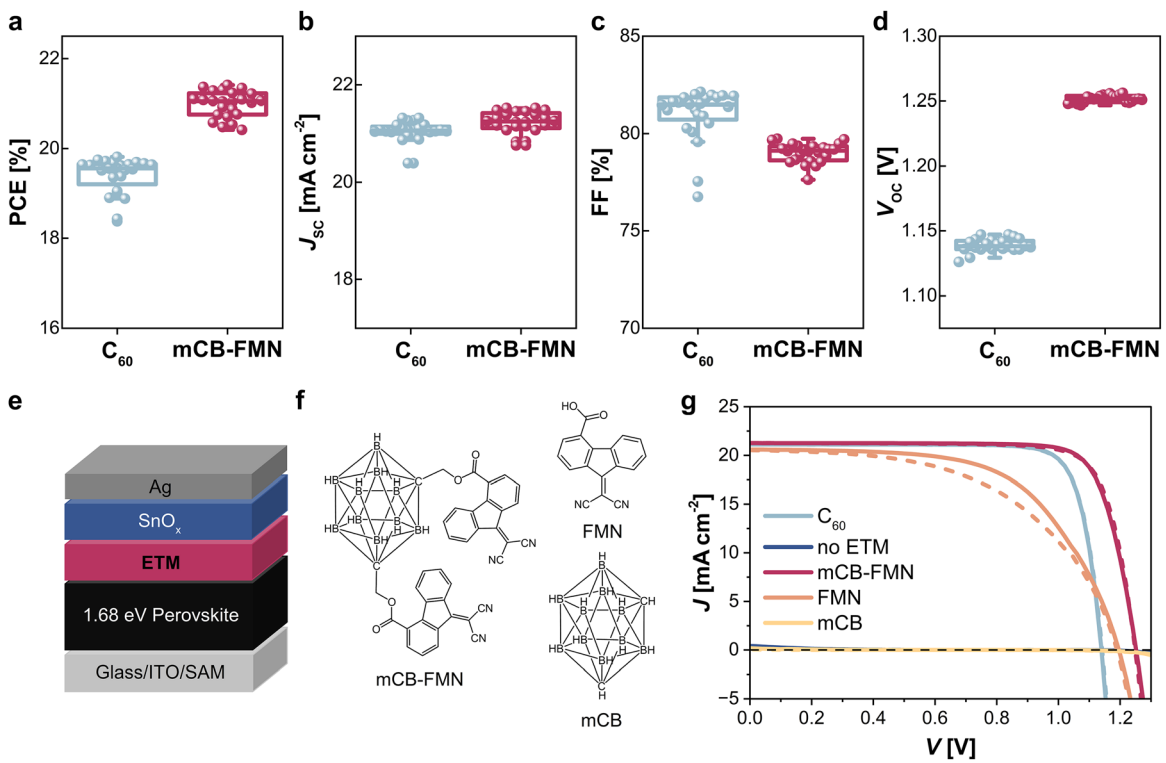

Fig. 3 Single-junction device results. Statistical representation of the (a) PCE, (b) J_{SC}, (c) FF, and (d) V_{OC} of opaque perovskite single-junction devices using 16 nm C_{60} or 4 nm mCB-FMN as ETM. The data represent forward and reverse J–V scans of 12 solar cells per variation. (e) Schematic of the opaque perovskite single-junction device stack. (f) Molecular structures of mCB-FMN and respective fragments – mCB and FMN – tested as ETMs in perovskite single-junction devices and (g) corresponding J–V curves in comparison to reference devices with C_{60} and without ETM. C_{60} and mCB-FMN were deposited *via* thermal evaporation, while FMN and mCB were spin-coated.

improved by 1.5% absolute (Fig. 3a). Under continuous maximum power point (MPP) tracking for 300 s, the PCE of devices with C_{60} decreased while it slightly increased for the solar cells with mCB-FMN, yielding stabilized PCEs of 19.8% and 21.4%, respectively (Fig. S28).

Semitransparent single-junction devices (0.16 cm^2 aperture area, illuminated through the ETM as in perovskite/silicon tandems) exhibited a similar V_{OC} gain of 110 mV compared to their C_{60}-based counterparts, as observed in opaque single-junctions, but additionally showed an increase in median J_{SC} by 0.8 mA cm^{-2} (Fig. S29). EQE measurements revealed that this gain originates from enhanced response at wavelengths below 600 nm (Fig. S30), which can be attributed to reduced parasitic absorption due to the thinner layer as well as the wide optical bandgap and lower absorption coefficient of mCB-FMN relative to C_{60}. These results highlight the strong potential of mCB-FMN for integration into tandem architectures.

To gain a deeper understanding of the working principle of mCB-FMN and to elucidate the functional contributions of its individual molecular components, we investigated opaque single-junction devices using spin-coated *meta*-carborane (mCB) and (4-carboxy-9-fluorenylidene)malononitrile (FMN) as isolated fragments of mCB-FMN (see molecular structure in Fig. 3f) as ETMs in comparison to the C_{60} reference and devices employing the full mCB-FMN molecule. Furthermore, devices without any ETM between the perovskite and SnO_x layer were included as control samples (no ETM). As shown in Fig. 3g and Fig. S31, devices without an ETM, as well as those employing mCB, exhibited no evidence of electron extraction. In contrast, devices with FMN as the ETM showed a distinct photovoltaic response, reflected in observable V_{OC} and J_{SC}, albeit with a low FF. These findings indicate that the FMN moiety plays a key role in facilitating charge extraction. This functionality can be attributed to the electron-accepting character of the FMN fragment.[31,32,65–67]

The results from the molecular fragment test further indicate that, although mCB did not function as an effective stand-alone ETM, its integration with the FMN functional groups critically influences the material's effectiveness as an ETM. To investigate this in more detail, we evaluated a series of ETMs incorporating the same FMN functional groups but using different carborane bodies, namely *ortho*- and *para*-carborane (oCB-FMN and pCB-FMN). The series also included a second variant of oCB-FMN (oCB-FMN-2), in which the CH_2 linker between the carborane core and the FMN unit is removed, resulting in a more rigid molecular geometry (Fig. S33a). TGA confirmed that all materials are suitable for deposition *via* thermal evaporation (Fig. S32a). Accordingly, devices were fabricated using evaporated ETM layers with the previously optimized thickness for mCB-FMN of 4 nm. XTOF measurements revealed that the oCB- and pCB-based ETMs exhibit slightly lower electron mobility than mCB-FMN, along with a more pronounced field dependence of the mobility (Fig. S32b and Table S4), which in organic semiconductors is typically associated with increased energetic disorder.[68] In solar cells, all ETMs resulted in charge extraction and showed similar J_{SC} and high median V_{OC} values between 1.23 and 1.25 V (Fig. S33b). The most pronounced differences were observed in the FF, which in comparison to mCB-FMN, was reduced for oCB-FMN and pCB-FMN, and further decreased in the case of oCB-FMN-2. Overall, the results confirm the central role of the FMN unit in enabling electron extraction, while also highlighting the importance of the choice of the carborane core and the positioning of the functional group, which likely influence molecular and energetic order and ultimately the optoelectronic properties. Moreover, the pronounced drop in electron mobility and device FF observed for oCB-FMN-2 indicates that not only the molecular core but also sufficient rotational flexibility of the functional groups is essential for ordered growth of the ETM film, facilitating efficient charge transport.

2.5. Proof-of-concept perovskite/silicon tandem solar cells

To evaluate the applicability of mCB-FMN in tandem architectures, we integrated the ETM into monolithic perovskite/silicon tandem solar cells employing a silicon heterojunction (SHJ) bottom cell with a planar front side (see the device stack in Fig. 4a). The tandem solar cells with C_{60} or mCB-FMN were fabricated under identical conditions, differing only in the ETM and its thickness. The resulting proof-of-concept devices yielded

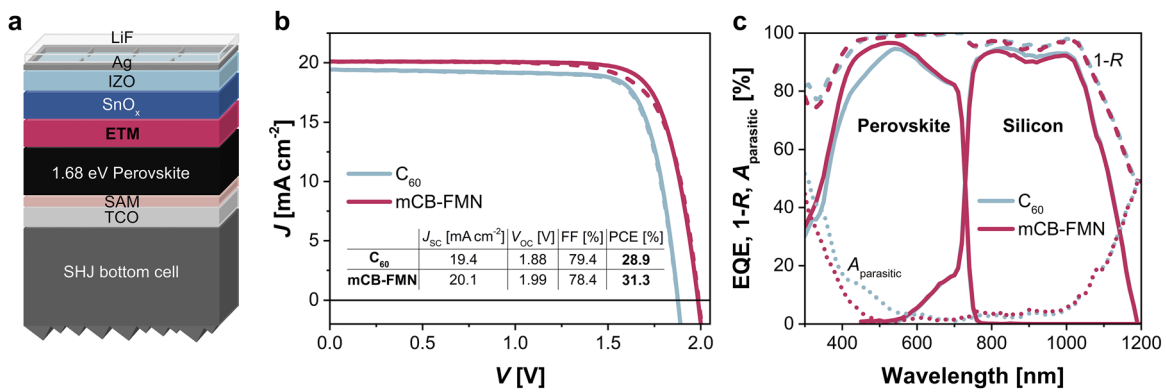

Fig. 4 Perovskite/silicon tandem solar cells. (a) Schematic of the perovskite/silicon tandem solar cell stack. (b) *J*–*V* curves and (c) corresponding EQE, 1-*R* and $A_{parasitic}$ of tandem solar cells with 4 nm mCB-FMN or 16 nm C_{60}. The integrated current densities of the top and bottom cells are 19.32 and 20.75 mA cm^{-2}, and 20.10 and 20.53 mA cm^{-2} for the devices with C_{60} and mCB-FMN, respectively.

reverse scan PCEs of 28.9% with 16 nm C_{60} and 31.3% with 4 nm mCB-FMN (Fig. 4b), with corresponding stabilized PCEs of 28.2% and 31.0% after 180 s of MPP tracking (Fig. S34b). The device with mCB-FMN showed a markedly increased V_{OC} of 1.99 V compared to 1.88 V with C_{60}, consistent with the trends observed in perovskite single-junction devices, even surpassing our reference tandem device employing a state-of-the-art piperazinium iodide (PI) surface treatment[10] for the perovskite/C_{60} interface (Fig. S34a). The V_{OC} gain of 110 mV was accompanied by a slight reduction in the FF, from 79.3% with C_{60} to 78.4% with mCB-FMN as the ETM, and a slight increase in hysteresis between forward and reverse scan. As shown in Fig. 4c, EQE measurements revealed an enhanced top-cell response between 350 and 600 nm for the mCB-FMN-based tandem device, translating into an integrated top cell current density of 20.09 mA cm^{-2} compared to 19.32 mA cm^{-2} with C_{60}, matching the results from semitransparent single-junction solar cells. Since the perovskite top cell is the current-limiting subcell in this tandem configuration, the EQE improvement was directly reflected in the J_{SC} from J–V measurements (increase of 0.7 mA cm^{-2}). Moreover, illumination intensity-dependent J–V measurements enabled the reconstruction of series resistance-free pseudo-J–V curves, indicating a higher FF potential for mCB-FMN (85.9%) compared to a device with C_{60} (85.0%), and a notably increased pseudo-PCE of 34.3% *versus* 31.0% (Fig. S35). These results highlight the substantial performance potential of mCB-FMN as an ETM in perovskite/silicon tandem solar cells.

2.6. Stability

We first tested the stability of mCB-FMN thin films deposited on quartz glass. Under 1-sun illumination and simultaneous heating to 85 °C, mCB-FMN showed superior stability compared to C_{60}: While the mCB-FMN thin films exhibited no changes in the transmission spectra even after 6 h, C_{60} layers showed signs of photopolymerization[69] already after 3 h under these conditions (Fig. 5a).

In the next step, we assessed the stability of mCB-FMN in solar cell partial stacks under ambient air exposure. We previously demonstrated that perovskite solar cell partial stacks featuring a passivated or treated and, thus low-loss perovskite/C_{60} interface, are highly susceptible to reversible degradation upon exposure to air or molecular oxygen, evidenced by a significant increase in non-radiative recombination.[23] We therefore compared the QFLS obtained from steady-state PL measurements under N_2 atmosphere and ambient air of solar cell partial stacks (glass/ITO/SAM/perovskite/ETM) with mCB-FMN to reference samples with a PI-treated perovskite/C_{60} interface. In an N_2 atmosphere, both sample types exhibited comparable QFLS values. However, while the samples with PI/C_{60} showed a drastic drop in QFLS of 90 meV when transitioning from N_2 to air, the samples with mCB-FMN demonstrated a minor decrease of only 20 meV (Fig. 5b). These findings suggest that O_2-induced degradation is largely mitigated in samples employing mCB-FMN. The improved interfacial stability under ambient conditions may enable more straightforward and reliable device processing and characterization.

Another form of instability frequently observed in perovskite solar cells with C_{60}, particularly when combined with surface treatments such as PI, is the deterioration of performance parameters with consecutive J–V scans. To assess the scan stability, we performed consecutive J–V measurements under 1-sun illumination on opaque single-junction devices. For reference devices with C_{60} and without additional surface treatment, a decrease in V_{OC} of 10 mV was observed over five scans, accompanied by an increase in FF (Fig. S36a). PI/C_{60}-based devices showed a pronounced drop in V_{OC} of 34 mV and an FF reduction by 1.5% (absolute) (Fig. S36b). Devices with mCB-FMN showed minimal changes, with V_{OC} and FF values of 1.258 V to 1.252 V and 79.3% to 79.0% in the first and fifth scan, respectively (Fig. S36c).

Although opaque single-junction devices with mCB-FMN as the ETM exhibited excellent scan stability, they showed faster

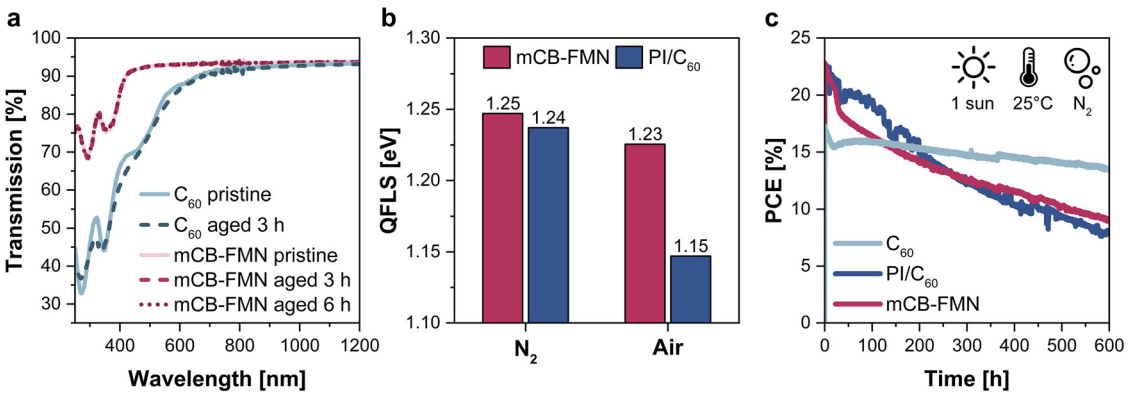

Fig. 5 Stability. (a) Spectral transmission of pristine and aged mCB-FMN and C_{60} thin films (15 nm) on quartz-glass. Ageing was performed in an N_2 atmosphere at 85 °C and under 1-sun equivalent illumination from an LED-based sun simulator (Wavelabs Sinus-300). (b) QFLS from steady-state PL measurements of solar cell partial stacks consisting of glass/ITO/SAM/perovskite/(passivation)/ETM with mCB-FMN and piperazinium iodide (PI)/C_{60}. The measurements were first conducted in N_2 atmosphere and subsequently in ambient air. (c) Mean MPP of opaque single-junction devices with C_{60} (9 solar cells), PI/C_{60} (6 solar cells), and mCB-FMN (11 cells) as ETM. The measurements were conducted under continuous 1-sun illumination at 25 °C, and in N_2 atmosphere.

degradation compared to reference devices with C_{60} under continuous MPP tracking for 600 h (Fig. 5c). While devices with C_{60} displayed a stable V_{MPP} and only a slight reduction in J_{MPP}, devices with mCB-FMN exhibited losses in both V_{MPP} and J_{MPP} (Fig. S37). The overall performance loss is comparable to that observed in devices with a PI-treated perovskite/C_{60} interface, which exhibit similar initial performance. This accelerated aging in devices with the novel ETM could originate from stack-specific degradation processes involving interactions between mCB-FMN and adjacent layers and/or from enhanced diffusion processes within the device promoted by the reduced ETM thickness.

To further investigate the degradation observed for devices employing mCB-FMN or C_{60}, we performed PL and XPS measurements on solar cell partial stacks (glass/ITO/SAM/perovskite/(4 nm C_{60} or mCB-FMN)) before and after ageing for 3 h under 1-sun illumination at 85 °C and open-circuit conditions (Fig. S38–S42). These conditions have been used before to successfully reproduce trends observed during MPP tracking of complete devices.[70] A detailed discussion of the PL and XPS results is provided in Note S11. The findings indicate that the reduced stability with mCB-FMN is not solely a consequence of the small ETM thickness but rather points to a fundamentally different degradation pathway at the perovskite/ETM interface, involving partial decomposition of mCB-FMN and chemical interaction with the perovskite. Importantly, XPS measurements of identically aged mCB-FMN layers deposited on glass/ITO substrates reveal only minor changes and show no signs of decomposition of the mCB-FMN molecule. This observation is consistent with the thin-film stability results shown in Fig. 5a and suggests that the perovskite plays an active role in initiating the decomposition of the ETM, whereas the ETM itself remains stable under PV-relevant conditions (elevated temperature and illumination) in the absence of external chemical agents. Accordingly, the results point toward a possible mitigation strategy based on spatially separating the ETM from the perovskite. Interfacial degradation has previously been suppressed in C_{60}-based devices by introducing thin spacer layers such as MgF_x, CaF_x or AlO_x at the perovskite/ETM interface,[71–74] an approach that may likewise be applicable to mCB-FMN-based devices and will be explored in future work. Alternatively, enhancing the chemical robustness of the ETM at the perovskite interface through structural modifications of the mCB-FMN molecule may provide an additional strategy for improving the long-term stability of mCB-FMN-based devices.

3. Conclusions

In this study, we introduced a novel carborane-based ETM for perovskite/silicon tandem solar cells. Optoelectronic material characterization demonstrated that thermally evaporated mCB-FMN provides favorable energetic alignment with the perovskite while exhibiting lower optical absorption than C_{60}. Extensive charge carrier dynamics investigations using trSPV, trPL, and steady-state PL revealed efficient electron extraction accompanied by strongly reduced non-radiative recombination losses in comparison to conventional C_{60}. Complementary DFT calculations suggested an interaction between the nitrile nitrogen of mCB-FMN and undercoordinated Pb^{2+} sites on the perovskite surface as well as Pb_I antisite defects, pointing toward a potential chemical passivation effect. Despite the small ETM thickness of only 4 nm used in devices, KPFM and SEM measurements indicated uniform electronic properties and the formation of a homogeneous mCB-FMN film on the perovskite surface. Moreover, mechanical adhesion tests showed increased tensile strength of the perovskite/ETM/SnO_x stack, likely linked to the improved SnO_x ALD nucleation observed in *in situ* ellipsometry, XPS measurements, and SEM imaging. In line with the findings from material and interface characterizations, integration into solar cells resulted in substantially increased V_{OC} values, as well as higher J_{SC}s in ETM-side illuminated devices, leading to a 2.4% absolute PCE improvement in proof-of-concept perovskite/silicon tandem solar cells compared to C_{60}. The molecule fragment study and carborane core variation conducted in this work further not only contribute to the understanding of the working principle of mCB-FMN but also provide guidance for the molecular design of potential future ETMs. While mCB-FMN results in superior device performance and exhibits improved material stability in thin films under illumination and heat, reduced sensitivity to air exposure, and excellent scan stability, its operational stability under continuous MPP tracking still lags behind the C_{60} reference devices. Our results indicate that this reduced stability originates from interfacial degradation processes at the perovskite/mCB-FMN interface, likely involving perovskite-induced chemical decomposition of the ETM, rather than an intrinsic instability of the mCB-FMN molecule itself. Further understanding and controlling these interfacial chemical interactions – for example through the introduction of spacer layers or targeted modifications to the molecule itself – will be essential to unlocking the full potential of mCB-FMN.

Conflicts of interest

There are no conflicts to declare.

Data availability

All data supporting the findings of this study are available within the article and its supplementary information (SI). Supplementary information is available. See DOI: https://doi.org/10.1039/d6ee01246a.

Additional data are available from the corresponding author upon reasonable request.

Acknowledgements

The authors acknowledge funding from the Helmholtz Association through the HySPRINT Innovation Lab and the HyPerCells Research School. Funding from the Federal Ministry of Research, Technology and Space (BMFTR) and the Helmholtz Association for the project *"Zeitenwende – Zukunftstechnologie*

Tandem-Solarzellen'' is acknowledged, as well as funding from BMFTR for the *Perowin* project (grant no. 03SF0631). The authors acknowledge funding from the project *''SHAPE''* funded by the Federal Ministry of Economic Affairs and Energy (BMWE) (grant no. 03EE1123CC) and from the project *''Supertandem''* funded by the European Union's Horizon Europe research and innovation program (grant no. 101075605). Part of this research was conducted within the framework of the Joint Lab GEN_FAB and supported by the Helmholtz Association through the Solar Technology Acceleration Platform (Solar TAP). D.M. and L.K. acknowledge funding from the German State of Lower Saxony through the project *''NextGenPV''* under the funding program *zukunft.niedersachsen*. W.M.B.d.A. and J.K. acknowledge funding from BMWE through the project PeroQ2 (grant no. 03EE1183B). K.M. acknowledges the Gauss Centre for Supercomputing e.V. for providing computing time on the GCS Supercomputer SuperMUC-NG and the Alexander von Humboldt Foundation for the research funding. Y.S. and M.C. acknowledge funding from SolarLab within SolarNL, a national research, innovation and industrial development program funded by the Netherlands National Growth Fund. S.W. and D.K.K acknowledge support from the UK Department for Science, Innovation and Technology (DSIT) through the National Measurement System. V.G. and T.M. acknowledge funding from the Science Council of Lithuania and the Ministry of Education, Science and Sports of the Republic of Lithuania from the state budget under the program *University Excellence Initiative* through the project *''Technological and Physical Sciences Excellence Centre (TiFEC)''* (grant no. S-A-UEI-23-1) and funding from *PEPPERONI* project (grant no. 101084251). This project is co-funded by the European Union. Views and opinions expressed are those of the author(s) only and do not necessarily reflect those of the European Union or the European Climate, Infrastructure and Environment Executive Agency (CINEA). Neither the European Union nor the granting authority can be held responsible for them. The project is also supported by the Swiss State Secretariat for Education, Research and Innovation (SERI). W.S., S.N., and T.T. acknowledge funding from JSPS KAKENHI (JP23H00292, JP26H02275). The authors thank K. Reimer, J. Beckedahl, M. Choyne, C. Ferber, M. Wittig, T. Lußky, and H. Heinz for the technical support in the HySPRINT Innovation Lab. The authors thank E.A. Jackson and H. Richter for conducting the cost estimation, and A. Miaskiewicz for technical support with scanning electron microscopy imaging.

References

1 H. Chen, C. Liu, J. Xu, A. Maxwell, W. Zhou, Y. Yang, Q. Zhou, A. S. R. Bati, H. Wan, Z. Wang, L. Zeng, J. Wang, P. Serles, Y. Liu, S. Teale, Y. Liu, M. I. Saidaminov, M. Li, N. Rolston, S. Hoogland, T. Filleter, M. G. Kanatzidis, B. Chen, Z. Ning and E. H. Sargent, *Science*, 2024, **384**, 189–193.

2 L. Jia, S. Xia, J. Li, Y. Qin, B. Pei, L. Ding, J. Yin, T. Du, Z. Fang, Y. Yin, J. Liu, Y. Yang, F. Zhang, X. Wu, Q. Li, S. Zhao, H. Zhang, Q. Li, Q. Jia, C. Liu, X. Gu, B. Liu, X. Dong, J. Liu, T. Liu, Y. Gao, M. Yang, S. Yin, X. Ru, H. Chen, B. Yang, Z. Zheng, W. Zhou, M. Dou, S. Wang, S. Gao, L. Chen, M. Qu, J. Lu, L. Fang, Y. Wang, H. Deng, J. Yu, X. Zhang, M. Li, X. Lang, C. Xiao, Q. Hu, C. Xue, L. Ning, Y. He, Z. Li, X. Xu and B. He, *Nature*, 2025, **644**, 912–919.

3 S. Hu, J. Wang, P. Zhao, J. Pascual, J. Wang, F. Rombach, A. Dasgupta, W. Liu, M. A. Truong, H. Zhu, M. Kober-Czerny, J. N. Drysdale, J. A. Smith, Z. Yuan, G. J. W. Aalbers, N. R. M. Schipper, J. Yao, K. Nakano, S.-H. Turren-Cruz, A. Dallmann, M. G. Christoforo, J. M. Ball, D. P. McMeekin, K.-A. Zaininger, Z. Liu, N. K. Noel, K. Tajima, W. Chen, M. Ehara, R. A. J. Janssen, A. Wakamiya and H. J. Snaith, *Nature*, 2024, **639**, 93–101.

4 Z. Liu, R. Lin, M. Wei, M. Yin, P. Wu, M. Li, L. Li, Y. Wang, G. Chen, V. Carnevali, L. Agosta, V. Slama, N. Lempesis, Z. Wang, M. Wang, Y. Deng, H. Luo, H. Gao, U. Rothlisberger, S. M. Zakeeruddin, X. Luo, Y. Liu, M. Grätzel and H. Tan, *Nat. Mater.*, 2025, **24**, 252–259.

5 F. Xu, E. Aydin, I. Yavuz, C. Deger, E. Ugur, J. Liu, X. Zhang, A. Razzaq, L. Xu, M. Marengo, B. Vishal, A. Prasetio, A. Subbiah, A. Pininti, T. Allen and S. De Wolf, *Nat. Mater.*, 2026, **25**, 259–266.

6 J. Siekmann, A. Kulkarni, S. Akel, B. Klingebiel, M. Saliba, U. Rau and T. Kirchartz, *Adv. Energy Mater.*, 2023, **13**, 2300448.

7 Z. Guan, Y. Li, P. Man, H. Tan, Q. Wei, J. Liu, M. Li, T. H. Ly, J. Yin and C.-S. Lee, *Adv. Mater.*, 2024, **36**, 2407406.

8 P.-W. Liang, C.-C. Chueh, S. T. Williams and A. K.-Y. Jen, *Adv. Energy Mater.*, 2015, **5**, 1402321.

9 A. A. Said, E. Aydin, E. Ugur, Z. Xu, C. Deger, B. Vishal, A. Vlk, P. Dally, B. K. Yildirim, R. Azmi, J. Liu, E. A. Jackson, H. M. Johnson, M. Gui, H. Richter, A. R. Pininti, H. Bristow, M. Babics, A. Razzaq, T. G. Allen, M. Ledinský, I. Yavuz, B. P. Rand and S. De Wolf, *Nat. Commun.*, 2024, **15**, 708.

10 S. Mariotti, E. Köhnen, F. Scheler, K. Sveinbjörnsson, L. Zimmermann, M. Piot, F. Yang, B. Li, J. Warby, A. Musiienko, D. Menzel, F. Lang, S. Keßler, I. Levine, D. Mantione, A. Al-Ashouri, M. S. Härtel, K. Xu, A. Cruz, J. Kurpiers, P. Wagner, H. Köbler, J. Li, A. Magomedov, D. Mecerreyes, E. Unger, A. Abate, M. Stolterfoht, B. Stannowski, R. Schlatmann, L. Korte and S. Albrecht, *Science*, 2023, **381**, 63–69.

11 X. Y. Chin, D. Turkay, J. A. Steele, S. Tabean, S. Eswara, M. Mensi, P. Fiala, C. M. Wolff, A. Paracchino, K. Artuk, D. Jacobs, Q. Guesnay, F. Sahli, G. Andreatta, M. Boccard, Q. Jeangros and C. Ballif, *Science*, 2023, **381**, 59–63.

12 E. Ugur, A. A. Said, P. Dally, S. Zhang, C. E. Petoukhoff, D. Rosas-Villalva, S. Zhumagali, B. K. Yildirim, A. Razzaq, S. Sarwade, A. Yazmaciyan, D. Baran, F. Laquai, C. Deger, I. Yavuz, T. G. Allen, E. Aydin and S. De Wolf, *Science*, 2024, **385**, 533–538.

13 J. Liu, Y. He, L. Ding, H. Zhang, Q. Li, L. Jia, J. Yu, T. W. Lau, M. Li, Y. Qin, X. Gu, F. Zhang, Q. Li, Y. Yang, S. Zhao, X. Wu, J. Liu, T. Liu, Y. Gao, Y. Wang, X. Dong, H. Chen, P. Li, T. Zhou, M. Yang, X. Ru, F. Peng, S. Yin, M. Qu, D. Zhao, Z. Zhao, M. Li, P. Guo, H. Yan, C. Xiao, P. Xiao, J. Yin, X. Zhang, Z. Li, B. He and X. Xu, *Nature*, 2024, **635**, 596–603.

14 F. Sahli, J. Werner, B. A. Kamino, M. Bräuninger, R. Monnard, B. Paviet-Salomon, L. Barraud, L. Ding,

J. J. Diaz Leon, D. Sacchetto, G. Cattaneo, M. Despeisse, M. Boccard, S. Nicolay, Q. Jeangros, B. Niesen and C. Ballif, *Nat. Mater.*, 2018, **17**, 820–826.
15 A. Al-Ashouri, E. Köhnen, B. Li, A. Magomedov, H. Hempel, P. Caprioglio, J. Marquez-Prieto, A. Vilches, E. Kasparavičius, J. Smith, N. Phung, D. Menzel, M. Grischek, L. Kegelmann, D. Skroblin, C. Gollwitzer, T. Malinauskas, M. Jošt, G. Matič and S. Albrecht, *Science*, 2020, **370**, 1300–1309.
16 P. Tockhorn, J. Sutter, A. Cruz, P. Wagner, K. Jäger, D. Yoo, F. Lang, M. Grischek, B. Li, J. Li, O. Shargaieva, E. Unger, A. Al-Ashouri, E. Köhnen, M. Stolterfoht, D. Neher, R. Schlatmann, B. Rech, B. Stannowski, S. Albrecht and C. Becker, *Nat. Nanotechnol.*, 2022, **17**, 1214–1221.
17 D. Turkay, K. Artuk, X.-Y. Chin, D. A. Jacobs, S.-J. Moon, A. Walter, M. Mensi, G. Andreatta, N. Blondiaux, H. Lai, F. Fu, M. Boccard, Q. Jeangros, C. M. Wolff and C. Ballif, *Joule*, 2024, **8**, 1735–1753.
18 J. Warby, F. Zu, S. Zeiske, E. Gutierrez-Partida, L. Frohloff, S. Kahmann, K. Frohna, E. Mosconi, E. Radicchi, F. Lang, S. Shah, F. Peña-Camargo, H. Hempel, T. Unold, N. Koch, A. Armin, F. De Angelis, S. D. Stranks, D. Neher and M. Stolterfoht, *Adv. Energy Mater.*, 2022, **12**, 2103567.
19 R. Zahran and Z. Hawash, *Adv. Mater. Interfaces*, 2022, **9**, 2201438.
20 H. Bristow, X. Li, M. Babics, S. Kosar, A. R. Pininti, S. Zhang, B. Vishal, S. Sarwade, A. Razzaq, A. A. Said, G. Lubineau and S. De Wolf, *Sol. RRL*, 2024, **8**, 2400289.
21 M. De Bastiani, G. Armaroli, R. Jalmood, L. Ferlauto, X. Li, R. Tao, G. T. Harrison, M. K. Eswaran, R. Azmi, M. Babics, A. S. Subbiah, E. Aydin, T. G. Allen, C. Combe, T. Cramer, D. Baran, U. Schwingenschlögl, G. Lubineau, D. Cavalcoli and S. De Wolf, *ACS Energy Lett.*, 2022, **7**, 827–833.
22 A. G. Kuba, C. Santiwipharat, R. J. Richardson, U. K. Das, K. D. Dobson and W. N. Shafarman, *ACS Appl. Energy Mater.*, 2024, **7**, 11921–11928.
23 L. Zimmermann, D. Menzel, R. Gundermann, M. Simmonds, F. Scheler, T. Gries, E. Nandayapa, A. F. Castro Mendez, F. Mathies, A. Miaskiewicz, E. J. W. List-Kratochvil, P. Holzhey, A. Musiienko, F. Lang, L. Korte, E. Köhnen and S. Albrecht, *Adv. Energy Mater.*, 2025, **15**, 2501225.
24 V. Sittinger, P. S. C. Schulze, C. Messmer, A. Pflug and J. C. Goldschmidt, *Opt. Express*, 2022, **30**, 37957–37970.
25 C. Gong, H. Li, Z. Xu, Y. Li, H. Wang, Q. Zhuang, A. Wang, Z. Li, Z. Guo, C. Zhang, B. Wang, X. Li and Z. Zang, *Nat. Commun.*, 2024, **15**, 9154.
26 J. L. Surel, P. Caprioglio, J. A. Smith, A. Dasgupta, F. Furlan, C. Henderson, F. Yang, B. M. Gallant, S. Seo, A. Knight, M. Kober-Czerny, J. Luke, D. P. McMeekin, A. I. Tartakovskii, J.-S. Kim, N. Gasparini and H. J. Snaith, *EES Sol.*, 2025, **1**, 567–579.
27 F. Scheler, S. Mariotti, D. Mantione, S. Shah, D. Menzel, H. Köbler, M. Simmonds, T. W. Gries, J. Kurpiers, V. Škorjanc, J. Li, A. Al-Ashouri, P. Wagner, S. P. Harvey, F. Yang, M. Rusu, T. Unold, B. Stannowski, K. Zhu, F. Lang, D. Neher, E. Unger, A. Abate, D. Mecerreyes, M. Stolterfoht, E. Köhnen, L. Korte, M. Topič and S. Albrecht, *Adv. Energy Mater.*, 2025, **15**, 2404726.
28 K. Frohna, C. Chosy, A. Al-Ashouri, F. Scheler, Y.-H. Chiang, M. Dubajic, J. E. Parker, J. M. Walker, L. Zimmermann, T. A. Selby, Y. Lu, B. Roose, S. Albrecht, M. Anaya and S. D. Stranks, *Nat. Energy*, 2025, **10**, 66–76.
29 K. Schutt, M. Davis, M. Li, S. A. Johnson, D. Martinez, J. Titus, T. Leijtens, B. Martin, M. D. McGehee, S. R. Marder, N. Rolston and J. M. Luther, *ACS Energy Lett.*, 2025, **10**, 6307–6317.
30 K. Feng, G. Wang, Q. Lian, S. Gámez-Valenzuela, B. Li, R. Ding, W. Yang, K. Wang, J. Zeng, Y. Zhang, S. Y. Jeong, B. Xu, A. Ho-Baillie, H. Y. Woo, A. Facchetti and X. Guo, *Nat. Mater.*, 2025, **24**, 770–777.
31 X. Huang, D. Xia, Q. Xie, D. Wang, Q. Li, C. Zhao, J. Yin, F. Cao, Z. Su, Z. Zeng, W. Jiang, W. Kaminsky, K. Liu, F. R. Lin, Q. Feng, B. Wu, S.-W. Tsang, D. Lei, W. Li and A. K.-Y. Jen, *Nat. Commun.*, 2025, **16**, 1626.
32 W. Yan, Z. He, J. Jiang, D. Lu, Y. Gong, W. Yang, R. Xia, W. Huang and H. Xin, *J. Mater. Chem. C*, 2020, **8**, 14773–14781.
33 A. A. Bizyaeva, A. F. Akbulatov, V. V. Ozerova, N. A. Emelianov, A. G. Buyanovskaya, L. A. Frolova, P. A. Troshin and S. A. Kuklin, *Dyes Pigm.*, 2024, **231**, 112427.
34 R. Zhu, Q.-S. Li and Z.-S. Li, *ACS Appl. Mater. Interfaces*, 2020, **12**, 38222–38231.
35 S.-K. Jung, J. H. Heo, D. W. Lee, S.-H. Lee, S.-C. Lee, W. Yoon, H. Yun, D. Kim, J. H. Kim, S. H. Im and O.-P. Kwon, *ChemSusChem*, 2019, **12**, 224–230.
36 J. H. Heo, S.-C. Lee, S.-K. Jung, O.-P. Kwon and S. H. Im, *J. Mater. Chem. A*, 2017, **5**, 20615–20622.
37 H. Wang, C. Zhang, Y. Yao, C. Cheng and K. Wang, *Small*, 2024, **20**, 2403193.
38 D. Zhao, Z. Zhu, M.-Y. Kuo, C.-C. Chueh and A. K.-Y. Jen, *Angew. Chem., Int. Ed.*, 2016, **55**, 8999–9003.
39 D. Gao, B. Li, Q. Liu, C. Zhang, Z. Yu, S. Li, J. Gong, L. Qian, F. Vanin, K. Schutt, M. A. Davis, A. F. Palmstrom, S. P. Harvey, N. J. Long, J. M. Luther, X. C. Zeng and Z. Zhu, *Science*, 2024, **386**, 187–192.
40 S. Y. Kim, M. Y. Woo, M. J. Jeong, S. W. Jeon, J. W. Ahn, J. H. Park, C. Y. Kim, D. H. Kim, O. J. Oh, G. Yu, S. Lee, C. Kim, D. H. Kim and J. H. Noh, *Adv. Energy Mater.*, 2024, **14**, 2402433.
41 F. Aniés, F. Furlan, Z. Qiao, V. Pirela, M. Bidwell, M. Rimmele, J. Martín, N. Gasparini and M. Heeney, *J. Mater. Chem. C*, 2023, **11**, 3989–3996.
42 R. Furue, T. Nishimoto, I. S. Park, J. Lee and T. Yasuda, *Angew. Chem., Int. Ed.*, 2016, **55**, 7171–7175.
43 K.-R. Wee, Y.-J. Cho, S. Jeong, S. Kwon, J.-D. Lee, I.-H. Suh and S. O. Kang, *J. Am. Chem. Soc.*, 2012, **134**, 17982–17990.
44 F. Aniés, I. Hamilton, C. S. P. De Castro, F. Furlan, A. V. Marsh, W. Xu, V. Pirela, A. Patel, M. Pompilio, F. Cacialli, J. Martín, J. R. Durrant, F. Laquai, N. Gasparini, D. D. C. Bradley and M. Heeney, *J. Am. Chem. Soc.*, 2024, **146**, 13607–13616.
45 J. Marshall, J. Hooton, Y. Han, A. Creamer, R. Shahid Ashraf, Y. Porte, T. D. Anthopoulos, P. N. Stavrinou, M. A. McLachlan, H. Bronstein, P. Beavis and M. Heeney, *Polym. Chem.*, 2014, **5**, 6190–6199.

46 F. Ye, S. Zhang, J. Warby, J. Wu, E. Gutierrez-Partida, F. Lang, S. Shah, E. Saglamkaya, B. Sun, F. Zu, S. Shoaee, H. Wang, B. Stiller, D. Neher, W.-H. Zhu, M. Stolterfoht and Y. Wu, *Nat. Commun.*, 2022, **13**, 7454.

47 Z. He, J. Xiong, Y. Zuo, H. Zhao, F. Liu, Q. Hu, Q. Yang, C. Zhou, L. Li, Q. Dai, H. Zhang, J. Zhang and J. Wang, *Adv. Mater.*, 2025, **37**, 2414155.

48 S. Tan, C. Li, C. Peng, W. Yan, H. Bu, H. Jiang, F. Yue, L. Zhang, H. Gao and Z. Zhou, *Nat. Commun.*, 2024, **15**, 4136.

49 B. G. Kim, W. Jang, H. Jeon, S. Lee, W.-S. Han and D. H. Wang, *Sol. Energy Mater. Sol. Cells*, 2020, **208**, 110414.

50 D. Menzel, A. Al-Ashouri, A. Tejada, I. Levine, J. A. Guerra, B. Rech, S. Albrecht and L. Korte, *Adv. Energy Mater.*, 2022, **12**, 2201109.

51 W. Xu, L. J. F. Hart, B. Moss, P. Caprioglio, T. J. Macdonald, F. Furlan, J. Panidi, R. D. J. Oliver, R. A. Pacalaj, M. Heeney, N. Gasparini, H. J. Snaith, P. R. F. Barnes and J. R. Durrant, *Adv. Energy Mater.*, 2023, **13**, 2301102.

52 S. M. Oner, E. Sezen, M. S. Yordanli, E. Karakoc, C. Deger and I. Yavuz, *J. Phys. Chem. Lett.*, 2022, **13**, 324–330.

53 N. Liu and C. Yam, *Phys. Chem. Chem. Phys.*, 2018, **20**, 6800–6804.

54 R. Wang, J. Xue, K.-L. Wang, Z.-K. Wang, Y. Luo, D. Fenning, G. Xu, S. Nuryyeva, T. Huang, Y. Zhao, J. L. Yang, J. Zhu, M. Wang, S. Tan, I. Yavuz, K. N. Houk and Y. Yang, *Science*, 2019, **366**, 1509–1513.

55 J. J. Cordell, M. Woodhouse and E. L. Warren, *Joule*, 2025, **9**, 101781.

56 L. A. Zafoschnig, S. Nold and J. C. Goldschmidt, *IEEE J. Photovolt.*, 2020, **10**, 1632–1641.

57 K. A. Bush, A. F. Palmstrom, Z. J. Yu, M. Boccard, R. Cheacharoen, J. P. Mailoa, D. P. McMeekin, R. L. Z. Hoye, C. D. Bailie, T. Leijtens, I. M. Peters, M. C. Minichetti, N. Rolston, R. Prasanna, S. Sofia, D. Harwood, W. Ma, F. Moghadam, H. J. Snaith, T. Buonassisi, Z. C. Holman, S. F. Bent and M. D. McGehee, *Nat. Energy*, 2017, **2**, 17009.

58 K. O. Brinkmann, J. Zhao, N. Pourdavoud, T. Becker, T. Hu, S. Olthof, K. Meerholz, L. Hoffmann, T. Gahlmann, R. Heiderhoff, M. F. Oszajca, N. A. Luechinger, D. Rogalla, Y. Chen, B. Cheng and T. Riedl, *Nat. Commun.*, 2017, **8**, 13938.

59 S. A. Johnson, K. P. White, J. Tong, S. You, A. Magomedov, B. W. Larson, D. Morales, R. Bramante, E. Dunphy, R. Tirawat, C. L. Perkins, J. Werner, G. Lahti, C. Velez, M. F. Toney, K. Zhu, M. D. McGehee, J. J. Berry and A. F. Palmstrom, *Joule*, 2023, **7**, 2873–2893.

60 B. Yu, F. Tang, Y. Yang, J. Huang, S. Wu, F. Lu, W. Duan, A. Lambertz, K. Ding and Y. Mai, *Adv. Mater.*, 2023, **35**, 2202447.

61 J. A. Raiford, C. C. Boyd, A. F. Palmstrom, E. J. Wolf, B. A. Fearon, J. J. Berry, M. D. McGehee and S. F. Bent, *Adv. Energy Mater.*, 2019, **9**, 1902353.

62 A. E. A. Bracesco, J. van Himste, W. M. M. Kessels, V. Zardetto and M. Creatore, *ACS Appl. Mater. Interfaces*, 2024, **16**, 59468–59476.

63 U. Erdil, M. Khenkin, W. M. Bernardes de Araujo, Q. Emery, I. Lauermann, V. Paraskeva, M. Norton, S. Vediappan, D. K. Kumar, R. K. Gupta, I. Visoly-Fisher, M. Hadjipanayi, G. E. Georghiou, R. Schlatmann, A. Abate, E. A. Katz and C. Ulbrich, *Energy Technol.*, 2025, **13**, 2401280.

64 U. Amornkitbamrung, Y. Xu, A. Gibson, C. Wang, Y. In, H. J. Jeong, R. Rhee and H. Shin, *Langmuir*, 2025, **41**, 21500–21508.

65 H. I. Kim, M.-J. Kim, K. Choi, C. Lim, Y.-H. Kim, S.-K. Kwon and T. Park, *Adv. Energy Mater.*, 2018, **8**, 1702872.

66 H. Wang, C. Zhao, Z. Burešová, F. Bureš and J. Liu, *J. Mater. Chem. A*, 2023, **11**, 3753–3770.

67 C. H. Y. Ho, H. Cao, Y. Lu, T.-K. Lau, S. H. Cheung, H.-W. Li, H. Yin, K. L. Chiu, L.-K. Ma, Y. Cheng, S.-W. Tsang, X. Lu, S. K. So and B. S. Ong, *J. Mater. Chem. A*, 2017, **5**, 23662–23670.

68 A. Karki, G.-J. A. H. Wetzelaer, G. N. M. Reddy, V. Nádaždy, M. Seifrid, F. Schauer, G. C. Bazan, B. F. Chmelka, P. W. M. Blom and T.-Q. Nguyen, *Adv. Funct. Mater.*, 2019, **29**, 1901109.

69 M. Kato, M. Nakaya, S. Watanabe, K. Okamoto and J. Onoe, *AIP Adv.*, 2021, **11**, 075227.

70 F. Scheler, Doctoral Dissertation, University of Ljubljana, 2025, PID: 20.500.12556/RUL-175169.

71 K. Artuk, D. Turkay, M. D. Mensi, J. A. Steele, D. A. Jacobs, M. Othman, X. Yu Chin, S.-J. Moon, A. N. Tiwari, A. Hessler-Wyser, Q. Jeangros, C. Ballif and C. M. Wolff, *Adv. Mater.*, 2024, **36**, 2311745.

72 J. Liu, M. De Bastiani, E. Aydin, G. T. Harrison, Y. Gao, R. R. Pradhan, M. K. Eswaran, M. Mandal, W. Yan, A. Seitkhan, M. Babics, A. S. Subbiah, E. Ugur, F. Xu, L. Xu, M. Wang, A. Ur Rehman, A. Razzaq, J. Kang, R. Azmi, A. A. Said, F. H. Isikgor, T. G. Allen, D. Andrienko, U. Schwingenschlögl, F. Laquai and S. De Wolf, *Science*, 2022, **377**, 302–306.

73 L. Fang, M. Ren, B. Li, X. Liu, S. Liang, J. Petermann, M. Gholipoor, T. Zhao, J. Sutter, P. Fassl, H. Weber, R. Niemann, L. Dai, R. Guo, U. Lemmer, F. Fertig and U. W. Paetzold, *Nat. Commun.*, 2025, **16**, 8881.

74 H. Liu, H. Meng, Q. Liu, K. Wang, C. Peng, X. Sun, S. Li, X. Wang, Q. Tian, L. Wang and S. Pang, *Small Methods*, 2026, e70670.